

Rethinking Keypoint Representations: Modeling Keypoints and Poses as Objects for Multi-Person Human Pose Estimation

William McNally Kanav Vats Alexander Wong John McPhee
 Systems Design Engineering, University of Waterloo
 Waterloo Artificial Intelligence Institute
 {wmcnally, k2vats, a28wong, mcphee}@uwaterloo.ca
<https://github.com/wmcnally/kapao>

Abstract

In keypoint estimation tasks such as human pose estimation, heatmap-based regression is the dominant approach despite possessing notable drawbacks: heatmaps intrinsically suffer from quantization error and require excessive computation to generate and post-process. Motivated to find a more efficient solution, we propose a new heatmap-free keypoint estimation method in which individual keypoints and sets of spatially related keypoints (i.e., poses) are modeled as objects within a dense single-stage anchor-based detection framework. Hence, we call our method **KAPAO** (pronounced “Ka-Pow!”) for **K**eypoint**A**nd **P**oses **A**s **O**bjects. We apply KAPAO to the problem of single-stage multi-person human pose estimation by simultaneously detecting human pose objects and keypoint objects and fusing the detections to exploit the strengths of both object representations. In experiments, we observe that KAPAO is significantly faster and more accurate than previous methods, which suffer greatly from heatmap post-processing. Moreover, the accuracy-speed trade-off is especially favourable in the practical setting when not using test-time augmentation. Our large model, KAPAO-L, achieves an AP of 70.6 on the Microsoft COCO Keypoints validation set without test-time augmentation while being 2.5× faster than the next best single-stage model, whose accuracy is 4.0 AP less. Furthermore, KAPAO excels in the presence of heavy occlusion. On the CrowdPose test set, KAPAO-L achieves new state-of-the-art accuracy for a single-stage method with an AP of 68.9.

1. Introduction

Keypoint estimation is a computer vision task that involves localizing points of interest in images. Emerging as one of the most highly researched topics in the computer vision literature, keypoint estimation plays an important role in several related applications, including human

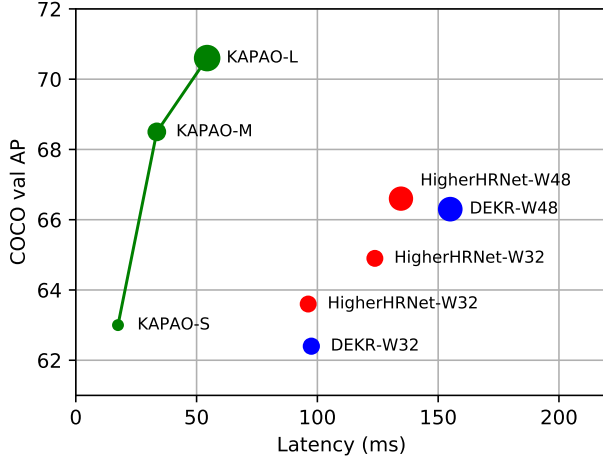


Figure 1. **Accuracy vs. Speed** – Comparison of our method KAPAO with state-of-the-art single-stage multi-person human pose estimation methods, DEKR [11] and HigherHRNet [6], without test-time augmentation (TTA). Raw data and more details are provided in Table 1. The circle size is proportional to the number of model parameters.

pose estimation [33, 42], hand pose estimation [16, 17], action recognition [10, 35, 36], object detection [64], multi-person tracking [1, 43], facial and object landmark detection [7, 18, 50, 58, 61], and sports analytics [34, 55].

The most common method for estimating keypoint locations involves generating target fields, referred to as *heatmaps*, by centering 2D Gaussians with small variances on the target keypoint coordinates. A deep convolutional neural network [23] is then used to regress the target heatmaps on the input images, and keypoint predictions are made via the arguments of the maxima of the predicted heatmaps [51]. If a peak in the heatmap surpasses a predefined confidence threshold, then a keypoint is detected.

While strong empirical results have positioned heatmap regression as the *de facto* standard method for detecting and localizing keypoints [4–6, 11, 21, 33, 39, 49, 51, 60, 62],



Figure 2. Screenshot from an inference video using KAPAO-S. The model runs in real-time on a TITAN Xp GPU, *i.e.*, faster than the native frame-rate of 25 frames per second. Face keypoints not shown. The demo is provided with our code.

there are several known drawbacks. First, these methods suffer from quantization error; the precision of a keypoint prediction is inherently limited by the spatial resolution of the heatmap. Larger heatmaps are therefore advantageous, but require additional upsampling operations and costly processing at higher resolutions [6, 33]. Even when large heatmaps are used, special post-processing steps are required to refine keypoint predictions, which can slow down inference [5, 6, 39]. Second, when two keypoints of the same type (*i.e.*, class) appear in close proximity to one another, the overlapping heatmap signals may be mistaken for a single keypoint. Indeed, this is a common failure case [4]. For these reasons, researchers have started investigating alternative, *heatmap-free* keypoint detection methods [24, 26, 27, 34, 61].

In this paper, we introduce a new heatmap-free keypoint detection method and apply it to single-stage multi-person human pose estimation. Our method builds on recent research showing how keypoints can be modeled as objects within a dense anchor-based detection framework by representing keypoints at the center of small square *keypoint bounding boxes* [34]. In preliminary experimentation with human pose estimation, we found that this keypoint detection approach works well for human keypoints that are characterized by local image features (*e.g.*, the eyes), but the same approach is less effective at detecting human keypoints that require a more global understanding (*e.g.*, the hips). We therefore introduce a new *pose object* representation to help detect sets of keypoints that are spatially related. In our overall approach, we detect keypoint objects and pose objects simultaneously and fuse the results using a simple matching algorithm to exploit the benefits of both object representations. By virtue of detecting pose objects, we unify person detection and keypoint estimation, leading to a highly efficient single-stage approach to multi-person human pose estimation.

Our approach, which we call KAPAO (for keypoints and poses as objects), builds on a recent implementation of the “You Only Look Once” (YOLO) dense detection frame-

work [2, 8, 44–46, 56], and includes a highly efficient network design that has been iteratively improved over several years of research and engineering. Moreover, because our method is not burdened by generating large and costly heatmaps that are subject to quantization error, it compares favourably against recent single-stage methods in terms of accuracy and inference speed, especially when not using test-time augmentation (TTA). As shown in Fig. 1, KAPAO achieves an AP of 70.6 on the Microsoft COCO Keypoints validation set without TTA, while being $2.5 \times$ faster than the next best model. Figure 2 shows a screenshot from a video inference using KAPAO-S, which runs in real-time on a TITAN Xp GPU. We summarize our research contributions:

- We propose a new object representation, called a *pose object*, which extends the conventional object representation by additionally including a set of keypoints associated with the object. We demonstrate how to learn the pose object representation using a multi-task loss.
- We develop a new approach to single-stage multi-person human pose estimation by simultaneously detecting *keypoint objects* and *human pose objects* and fusing the predictions. Compared to state-of-the-art methods, which all use heatmaps, our heatmap-free method is significantly faster and more accurate on two popular benchmark datasets: Microsoft COCO Keypoints and CrowdPose.

2. Related Work

Heatmap-free Keypoint Detection. Coincidentally, the first application of deep learning to human pose estimation did not use heatmaps. DeepPose [52] regressed keypoint coordinates directly from images using a cascade of deep neural networks that iteratively refined the keypoint predictions. Shortly thereafter, Tompson *et al.* [51] introduced keypoint heatmaps, hypothesizing that the direct regression of pose vectors from images was a difficult mapping to learn. Since then, heatmap regression has remained prevalent in human pose estimation [4–6, 11, 21, 33, 39, 49, 59, 60, 62], as well as other keypoint estimation applications [7, 16, 17, 53, 54, 58]. Nevertheless, the shortcomings of heatmaps have recently triggered research into new, heatmap-free keypoint detection methods.

Remarkably the computational inefficiencies associated with generating heatmaps and the inherent issue of quantization error, Li *et al.* [27] proposed to disentangle the horizontal and vertical keypoint coordinates such that each coordinate was represented using a one-hot encoded vector. This representation saved computation and permitted an expansion of the output resolution, thereby reducing the effects of quantization error and eliminating the

need for refinement post-processing. Li *et al.* [24] introduced the residual log-likelihood (RLE), a novel loss for direct keypoint regression based on normalizing flows [48], and matched the accuracy of state-of-the-art heatmap-based methods. Direct keypoint regression has also been attempted using Transformers [26].

Outside the realm of human pose estimation, Xu *et al.* [61] regressed anchor templates of facial keypoints and aggregated them to achieve state-of-the-art accuracy in facial alignment. In sports analytics, McNally *et al.* [34] encountered the issue of overlapping heatmap signals in the development of an automatic scoring system for darts, and therefore chose to model keypoints as objects using small square bounding boxes. This keypoint representation proved to be highly successful, and serves as the inspiration for our work.

Single-stage Human Pose Estimation. Methods for 2D human pose estimation generally fall into two categories: single-stage methods [4, 6, 11, 15, 22, 38, 40], and two-stage methods [5, 21, 33, 39, 49, 59, 60]. Two-stage methods detect the people in an image using an off-the-shelf person detector (*e.g.*, Faster R-CNN [47], YOLOv3 [46], etc.) and the poses are estimated for each person detection. For this reason, two-stage methods are frequently referred to as being *top-down*. In contrast, single-stage methods predict the poses of every person in an image following a single forward pass through a single network. Single-stage approaches may unify person detection and keypoint estimation, which is similar to our work and Mask R-CNN [15], an object detection network that was extended to perform keypoint estimation using one-hot segmentation masks. Alternatively, single-stage methods may detect all the keypoints in an image and perform a *bottom-up* grouping into distinct human poses [4, 6, 38]. Single-stage methods are less accurate than their two-stage counterparts, but usually perform better in crowded scenes [25] and are often preferred because of their simplicity and efficiency, which becomes particularly favourable as the number of people in the image increases.

In a seminal work among single-stage methods, Cao *et al.* [4] introduce a non-parametric representation called part affinity fields to encode the orientation of human limbs. They jointly learn keypoint locations and part affinity fields via heatmaps to enable a greedy bottom-up parsing of human poses. Newell *et al.* [38] perform single-stage multi-person human pose estimation by predicting associative embedding tags along with keypoint heatmaps, where keypoints with similar tag values are grouped into a pose. Nie *et al.* [40] introduced a new representation termed Structured Pose Representation (SPR) by incorporating a root keypoint for each person and encoding the relative positions of the remaining keypoints via displacement maps. Kreiss *et al.* [22] extended the concept of part affinity fields to esti-

mate composite fields called Part Intensity Fields (Pif) and Part Association Fields (Paf). With the incorporation of a scale dependent Laplacian L1 loss [20], their approach outperformed previous methods on low resolution images.

Cheng *et al.* [6] addressed the scale variation problem in single-stage human pose estimation with HigherHRNet, which used high resolution feature pyramids with multi-resolution supervision during training and multi-resolution heatmap aggregation during inference. Geng *et al.* [11] introduced a new disentangled keypoint representation (DEKR) that used adaptive convolutions and decoupling of one keypoint from others so that each representation focused on the corresponding keypoint region. HigherHRNet [6] and DEKR [11] provide similar performance and represent the state-of-the-art for single-stage human pose estimation at the time of writing.

Single-stage Object Detection. Deep learning-based object detection models can be categorized into two groups based on whether they use one or two stages. Two-stage detectors, popularized by the R-CNN family [3, 12, 13, 15, 47], generate a sparse set of candidate object locations in the first stage and classify each candidate into a foreground object class or background in the second stage. The more recent single-stage detectors unify the process by simultaneously classifying objects and regressing their locations over a dense grid. Popular single-stage object detectors include the Single Shot MultiBox Detector (SSD) [31], and YOLO [2, 44–46, 56].

Initially, single-stage object detectors were considered to be a justifiable trade-off; they provided lower accuracy but much better computational efficiency compared to two-stage detectors. However, Lin *et al.* [29] discovered that the extreme foreground-background class imbalance was destabilizing training. They proposed the Focal Loss to remedy the issue and used it to surpass the accuracy of all existing two-stage detectors while matching the speed of previous single-stage detectors. Recent iterations of the YOLO detector have also surpassed the accuracy of two-stage detectors [2, 46, 56].

Analogous to object detection, single-stage human pose estimation methods have the potential to be much faster than their two-stage counterparts. However, current state-of-the-art single-stage human pose estimations are heavily burdened by the processing of large heatmaps. As a result, their inference speed leaves much to be desired. This is especially true when TTA is used, which seems to be key to achieving good accuracy with heatmap-based methods. For example, we find that HigherHRNet [6] and DEKR [11] both run at a speed of less than one frame per second on a TITAN Xp GPU.

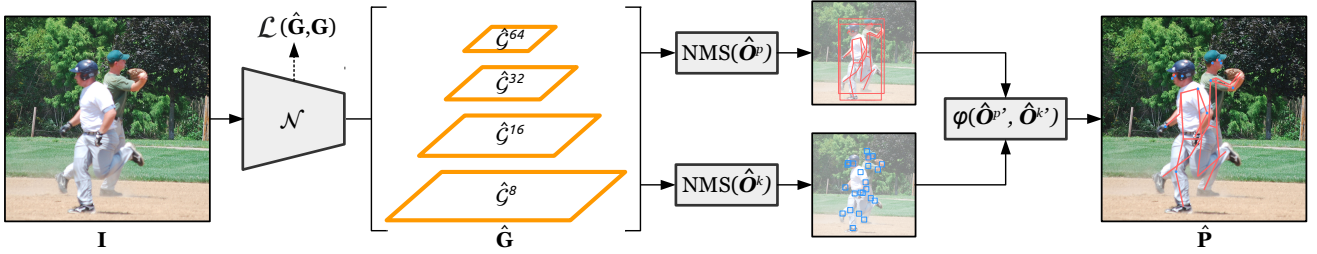


Figure 3. KAPAO uses a dense detection network \mathcal{N} trained using the multi-task loss \mathcal{L} to map an RGB image \mathbf{I} to a set of output grids $\hat{\mathbf{G}}$ containing the predicted pose objects $\hat{\mathbf{O}}^p$ and keypoint objects $\hat{\mathbf{O}}^k$. Non-maximum suppression (NMS) is used to obtain candidate detections $\hat{\mathbf{O}}^{p'}$ and $\hat{\mathbf{O}}^{k'}$, which are fused together using a matching algorithm φ to obtain the final human pose predictions $\hat{\mathbf{P}}$. The N_a and N_o dimensions in $\hat{\mathbf{G}}$ are not shown for clarity.

3. KAPAO

In our proposed approach to multi-person human pose estimation, we train a dense detection network to simultaneously predict a set of keypoint objects $\{\hat{\mathbf{O}}^k \in \hat{\mathbf{O}}^k\}$ and a set of pose objects $\{\hat{\mathbf{O}}^p \in \hat{\mathbf{O}}^p\}$, collectively $\hat{\mathbf{O}} = \hat{\mathbf{O}}^k \cup \hat{\mathbf{O}}^p$. We briefly introduce the concept behind each object type and the relevant notation. All units are assumed to be in pixels unless stated otherwise.

A keypoint object \mathcal{O}^k is an adaptation of the conventional object representation in which the coordinates of a keypoint are represented at the center (b_x, b_y) of a small bounding box \mathbf{b} with equal width b_w and height b_h : $\mathbf{b} = (b_x, b_y, b_w, b_h)$. The hyperparameter b_s is the keypoint bounding box size (*i.e.*, $b_s = b_w = b_h$). There are K classes of keypoint objects, one for each keypoint type in the labeled dataset [34].

Generally speaking, we consider a pose object \mathcal{O}^p to be an extension of the conventional object representation that additionally includes a set of keypoints associated with the object. While we envision pose objects being useful in related tasks such as facial and object landmark detection [19, 61], we apply pose objects to human pose estimation via detection of *human pose objects*, comprising a bounding box of class “person,” and a set of keypoints $\mathbf{z} = \{(x_k, y_k)\}_{k=1}^K$ that coincide with anatomical landmarks.

Both object representations possess unique advantages. Keypoint objects are specialized for the detection of individual keypoints that are characterized by strong local features. Examples of such keypoints that are common in human pose estimation include the eyes, ears and nose. However, keypoint objects carry no information regarding a person or pose. If used on their own for multi-person human pose estimation, a bottom-up grouping method would be needed to parse the detected keypoints into human poses. In contrast, pose objects are better suited for localizing keypoints with weak local features as they enable the network to learn the spatial relationships within a set of keypoints. Moreover, they can be leveraged for multi-person human pose estimation directly without the need for bottom-up parsing.

Recognizing that keypoint objects exist in a subspace of a pose objects, we design a network to simultaneously detect both object types with minimal computational overhead using a single, shared network head. During inference, the more precise keypoint object detections are fused with the human pose detections using a simple tolerance-based matching algorithm that improves the accuracy of the human pose predictions without sacrificing any significant amount of inference speed. The following sections provide details on the network architecture, the loss function used to train the network, and inference.

3.1. Architectural Details

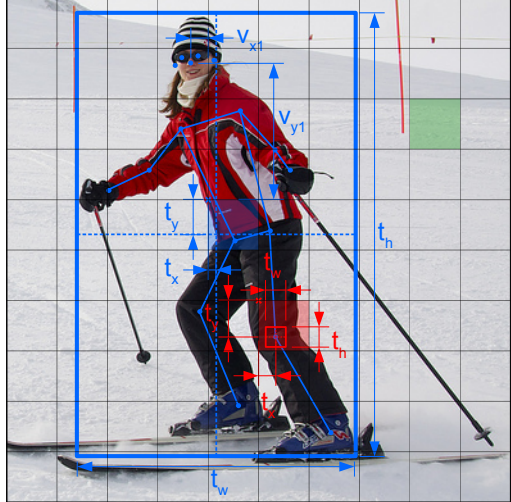
A diagram of KAPAO is provided in Figure 3. It uses a deep convolutional neural network \mathcal{N} to map an RGB input image $\mathbf{I} \in \mathbb{R}^{h \times w \times 3}$ to a set of four output grids $\hat{\mathbf{G}} = \{\hat{\mathcal{G}}^s\}$ containing the object predictions $\hat{\mathbf{O}}$, where $s \in \{8, 16, 32, 64\}$ and $\hat{\mathcal{G}}^s \in \mathbb{R}^{\frac{h}{s} \times \frac{w}{s} \times N_a \times N_o}$:

$$\mathcal{N}(\mathbf{I}) = \hat{\mathbf{G}}. \quad (1)$$

N_a is the number of anchor channels and N_o is the number of output channels for each object. \mathcal{N} is a YOLO-style feature extractor that makes extensive use of Cross-Stage-Partial (CSP) bottlenecks [57] within a feature pyramid [28] architecture. To provide flexibility for different speed requirements, we train three sizes of KAPAO models (*i.e.* S, M, L) by scaling the number of layers and channels in \mathcal{N} [8, 56].

Due to the nature of strided convolutions, the features in an output grid cell $\hat{\mathcal{G}}_{i,j}^s$ are conditioned on the image patch $\mathbf{I}_p = \mathbf{I}_{s:i \times s:j:(j+1)}$. Therefore, if the center of a target object (b_x, b_y) is situated in \mathbf{I}_p , the output grid cell $\hat{\mathcal{G}}_{i,j}^s$ is responsible for detecting it. The receptive field of an output grid increases with s , so smaller output grids are better suited for detecting larger objects.

Each output grid cell $\hat{\mathcal{G}}_{i,j}^s$ contains N_a anchor channels corresponding to anchor boxes $\mathbf{A}^s = \{(A_{w_a}, A_{h_a})\}_{a=1}^{N_a}$. A target object \mathcal{O} is assigned to an anchor channel via tolerance-based matching of the object and anchor box sizes. This provides redundancy such that a single grid cell $\hat{\mathcal{G}}_{i,j}^s$ can detect multiple objects, and enables specialization



grid cell target		$y = \left[p_o, t_x, t_y, t_w, t_h, c_1, \dots, c_{K+1}, v_{x1}, v_{y1}, \dots, v_{xK}, v_{yK} \right]$
human pose object		$y = \left[1, 0.2, 0.7, 5.5, 8.8, 1, 0, \dots, 0, -0.4, 3.7, \dots, 0.6, -4.1 \right]$ <small>$p_o, t_x, t_y, t_w, t_h, c_1, c_2, c_{K+1}, v_{x1}, v_{y1}, v_{xK}, v_{yK}$</small>
keypoint object		$y = \left[1, 0.3, 0.7, 0.4, 0.4, 0, 0, \dots, 1, \dots, 0, ?, ?, \dots, ?, ? \right]$ <small>$p_o, t_x, t_y, t_w, t_h, c_1, c_2, c_{15}, c_{K+1}, v_{x1}, v_{y1}, v_{xK}, v_{yK}$</small>
no object		$y = \left[0, ?, ?, \dots, ?, ? \right]$ <small>$p_o, t_x, t_y, v_{xK}, v_{yK}$</small>

Figure 4. Sample targets for a human pose object (blue), keypoint object (red), and no object (green). The “?” values are not used in the loss computation.

for different object sizes. Additional detection redundancy is provided by also allowing the neighbouring grid cells $\hat{G}_{i\pm 1,j}^s$ and $\hat{G}_{i,j\pm 1}^s$ to detect an object in \mathbf{I}_p [8, 56].

The N_o output channels of $\hat{G}_{i,j,a}^s$ contain the properties of a predicted object \hat{O} , including the “objectness” \hat{p}_o , or the probability that an object exists, the intermediate bounding boxes $\hat{\mathbf{t}}' = (\hat{t}_x', \hat{t}_y', \hat{t}_w', \hat{t}_h')$, the object class scores $\hat{\mathbf{c}} = (\hat{c}_1, \dots, \hat{c}_{K+1})$, and the intermediate keypoints $\hat{\mathbf{v}}' = \{(\hat{v}'_{xk}, \hat{v}'_{yk})\}_{k=1}^K$ for the human pose objects. Hence, $N_o = 3K + 6$.

Following [8, 56], an object’s bounding box $\hat{\mathbf{t}}$ is predicted in the grid coordinates and relative to the grid cell origin (i, j) using:

$$\hat{t}_x = 2\sigma(\hat{t}'_x) - 0.5 \quad \hat{t}_y = 2\sigma(\hat{t}'_y) - 0.5 \quad (2)$$

$$\hat{t}_w = \frac{A_w}{s}(2\sigma(\hat{t}'_w))^2 \quad \hat{t}_h = \frac{A_w}{s}(2\sigma(\hat{t}'_h))^2. \quad (3)$$

We extend this detection strategy to the keypoints of a pose object. A pose object’s keypoints $\hat{\mathbf{v}}$ are predicted in the grid coordinates and relative to the grid cell origin (i, j) using:

$$\hat{v}_{xk} = \frac{A_w}{s}(4\sigma(\hat{v}'_{xk}) - 2) \quad \hat{v}_{yk} = \frac{A_w}{s}(4\sigma(\hat{v}'_{yk}) - 2). \quad (4)$$

The sigmoid function σ is used to facilitate learning by constraining the ranges of the object properties (e.g., \hat{v}_{xk} and \hat{v}_{yk} are constrained to $\pm 2\frac{A_w}{s}$ and $\pm 2\frac{A_h}{s}$, respectively). To learn $\hat{\mathbf{t}}$ and $\hat{\mathbf{v}}$, losses are applied in the grid space. Sample targets \mathbf{t} and \mathbf{v} are shown in Figure 4.

3.2. Loss Function

A target set of grids \mathbf{G} is constructed and a multi-task loss $\mathcal{L}(\mathbf{G}, \mathbf{G})$ is applied to learn \hat{p}_o (\mathcal{L}_{obj}), $\hat{\mathbf{t}}$ (\mathcal{L}_{box}), $\hat{\mathbf{c}}$ (\mathcal{L}_{cls}), and $\hat{\mathbf{v}}$ (\mathcal{L}_{kps}) if the object is a pose object. The loss components are computed for a single image as follows:

$$\mathcal{L}_{obj} = \sum_s \frac{\omega_s}{n(G^s)} \sum_{G^s} \text{BCE}(\hat{p}_o, p_o) \cdot \text{IoU}(\hat{\mathbf{t}}, \mathbf{t}) \quad (5)$$

$$\mathcal{L}_{box} = \sum_s \frac{1}{n(\mathcal{O} \in G^s)} \sum_{\mathcal{O} \in G^s} 1 - \text{IoU}(\hat{\mathbf{t}}, \mathbf{t}) \quad (6)$$

$$\mathcal{L}_{cls} = \sum_s \frac{1}{n(\mathcal{O} \in G^s)} \sum_{\mathcal{O} \in G^s} \text{BCE}(\hat{\mathbf{c}}, \mathbf{c}) \quad (7)$$

$$\mathcal{L}_{kps} = \sum_s \frac{1}{n(\mathcal{O}^p \in G^s)} \sum_{\mathcal{O}^p \in G^s} \sum_{k=1}^K \delta(\nu_k > 0) \|\hat{\mathbf{v}}_k - \mathbf{v}_k\|_2 \quad (8)$$

where ω_s is the grid weighting, BCE is the binary cross-entropy, IoU is the complete intersection over union (CIoU) [63], and ν_k is the visibility flag of the target keypoint \mathbf{v}_k . When $\mathcal{G}_{i,j,a}^s$ is a target object \mathcal{O} , the target objectness $p_o = 1$ is multiplied by the IoU score to promote specialization amongst the anchor channel predictions. When $\mathcal{G}_{i,j,a}^s$ is not a target object, $p_o = 0$. In practice, we apply the losses over a batch of images using the batched grids. The total loss \mathcal{L} is a weighted summation of the loss components, scaled by the batch size N_b :

$$\mathcal{L} = N_b(\lambda_{obj}\mathcal{L}_{obj} + \lambda_{box}\mathcal{L}_{box} + \lambda_{cls}\mathcal{L}_{cls} + \lambda_{kps}\mathcal{L}_{kps}). \quad (9)$$

3.3. Inference

The predicted bounding boxes $\hat{\mathbf{t}}$ and keypoints $\hat{\mathbf{v}}$ are mapped back to the original image coordinates using the following transformation:

$$\hat{\mathbf{b}} = s(\hat{\mathbf{t}} + (i, j, 0, 0)) \quad \hat{\mathbf{z}}_k = s(\hat{\mathbf{v}}_k + (i, j)). \quad (10)$$

$\hat{G}_{i,j,a}^s$ represents a positive pose object detection \hat{O}^p if its confidence $\hat{p}_o \cdot \max(\hat{\mathbf{c}})$ is greater than a threshold τ_{cp} , and $\arg \max(\hat{\mathbf{c}}) = 1$. Similarly, $\hat{G}_{i,j,a}^s$ represents a positive keypoint object detection \hat{O}^k if $\hat{p}_o \cdot \max(\hat{\mathbf{c}}) > \tau_{ck}$ and $\arg \max(\hat{\mathbf{c}}) \neq 1$, where the keypoint object class is $\arg \max(\hat{\mathbf{c}}) - 1$.

To remove redundant detections and obtain the candidate pose objects $\hat{O}^{p'}$ and keypoint objects $\hat{O}^{k'}$, the positive pose object detections \hat{O}^p and positive keypoint object

Algorithm 1: Keypoint Object Fusion (φ)

```

Input:  $\hat{\mathbf{O}}^{p'}$ ,  $\hat{\mathbf{O}}^{k'}$ ,  $\tau_{fd}$ ,  $\tau_{fc}$ 
Output:  $\hat{\mathbf{P}}$ 
if  $n(\hat{\mathbf{O}}^{p'}) > 0$  then
    // initialize
     $\hat{\mathbf{P}} \leftarrow \{0_{K \times 3} \mid \_ \in \{1 \dots n(\hat{\mathbf{O}}^{p'})\}\} \text{ // poses}$ 
     $\zeta \leftarrow \{0 \mid \_ \in \{1 \dots n(\hat{\mathbf{O}}^{p'})\}\} \text{ // pose conf}$ 
    for  $(i, \hat{\mathbf{O}}^p) \in \text{enumerate}(\hat{\mathbf{O}}^{p'})$  do
         $\zeta_i = \hat{\mathbf{O}}_{p_o}^p \cdot \max(\hat{\mathbf{O}}_c^p)$ 
        for  $k \in \{1 \dots K\}$  do
             $\hat{\mathbf{P}}_i[k] \leftarrow (\hat{\mathbf{O}}_{x_k}^p, \hat{\mathbf{O}}_{y_k}^p, 0)$ 
         $\hat{\mathbf{P}}^* \leftarrow \{\hat{\mathbf{P}}_i \in \hat{\mathbf{P}} \mid \zeta_i > \tau_{fc}\}$ 
        if  $n(\hat{\mathbf{P}}^*) > 0 \wedge n(\hat{\mathbf{O}}^{k'}) > 0$  then
            for  $\hat{\mathbf{O}}^k \in \hat{\mathbf{O}}^{k'}$  do
                 $k \leftarrow \arg \max(\hat{\mathbf{O}}_c^k) - 1$ 
                 $\mathbf{d}_i \leftarrow \|\hat{\mathbf{P}}^*[k, [1, 2]] - (\hat{\mathbf{O}}_{b_x}^k, \hat{\mathbf{O}}_{b_y}^k)\|_2$ 
                 $m = \arg \min(\mathbf{d}) \text{ // match index}$ 
                if  $\mathbf{d}_m < \tau_{fd} \wedge \hat{\mathbf{P}}^*[k, 3] < \max(\hat{\mathbf{O}}_c^k)$  then
                     $\hat{\mathbf{P}}^*[k] = (\hat{\mathbf{O}}_{b_x}^k, \hat{\mathbf{O}}_{b_y}^k, \max(\hat{\mathbf{O}}_c^k))$ 
        else
             $\hat{\mathbf{P}} = \emptyset \text{ // empty set}$ 


---



```

detections $\hat{\mathbf{O}}^p$ are filtered using non-maximum suppression (NMS) with the IoU thresholds τ_{bp} and τ_{bk} :

$$\hat{\mathbf{O}}^{p'} = \text{NMS}(\hat{\mathbf{O}}^p, \tau_{bp}) \quad \hat{\mathbf{O}}^{k'} = \text{NMS}(\hat{\mathbf{O}}^k, \tau_{bk}). \quad (11)$$

Finally, the human pose predictions $\hat{\mathbf{P}} = \{\hat{\mathbf{P}}_i \in \mathbb{R}^{K \times 3}\}$ for $i \in \{1 \dots n(\hat{\mathbf{O}}^{p'})\}$ are obtained by fusing the candidate keypoint objects with the candidate pose objects using a distance tolerance τ_{fd} . To promote correct matches of keypoint objects to poses, the keypoint objects are only fused to pose objects with $\hat{p}_o \cdot \max(\hat{\mathbf{c}}) > \tau_{fc}$:

$$\hat{\mathbf{P}} = \varphi(\hat{\mathbf{O}}^{p'}, \hat{\mathbf{O}}^{k'}, \tau_{fd}, \tau_{fc}). \quad (12)$$

The keypoint object fusion function φ is provided in Algorithm 1, where we use the following notation to index an object's properties: $x = \mathcal{O}_x$ (e.g., a pose object's keypoints $\hat{\mathbf{z}} = \hat{\mathbf{O}}_z^{p'}$).

3.4. Limitations

A limitation of our method is that pose objects do not include individual keypoint confidences, so the human pose predictions typically contain a sparse set of keypoint confidences $\hat{\mathbf{P}}_i[:, 3]$ populated by the fused keypoint objects (see Algorithm 1 for details). If desired, a complete set of keypoint confidences can be induced by only using keypoint objects, which is realized when $\tau_{ck} \rightarrow 0$. Another limitation is that training requires a considerable amount of compute due to the large input size used.

4. Experiments

We evaluate KAPAO on two multi-person human pose estimation datasets: COCO Keypoints [30] and CrowdPose [25], and compare our results against state-of-the-art methods. PyTorch 1.9 was used for implementation. All hyperparameters are provided in the source code.

4.1. COCO Keypoints

Microsoft COCO Keypoints is a large-scale multi-person human pose estimation dataset containing over 200k images and 250k person instances with 17 keypoints ($K=17$). We train on the `train2017` split, containing 118k images and 150k person instances, and validate on the 5k images in `val2017`. We also evaluate on the `test-dev` split, which contains 20k images. For accuracy metrics, we report the average precision (AP) and average recall (AR) scores based on the Object Keypoint Similarity (OKS)¹: AP (mean AP over OKS $\in \{0.50, 0.55, \dots, 0.95\}$), AP⁵⁰ (AP at OKS = 0.50), AP⁷⁵, AP^M (medium objects), AP^L (large objects), and AR (mean AR over OKS $\in \{0.50, 0.55, \dots, 0.95\}$).

Training. All models were trained for 500 epochs using stochastic gradient descent with Nesterov momentum [37], weight decay, and a learning rate decayed over a single cosine cycle [32] with a 3-epoch warm-up period [14]. The input images were resized and padded to 1280×1280 , keeping the original aspect ratio. Data augmentation used during training included mosaic [2], HSV color-space perturbations, horizontal flipping, translations, and scaling.

Many of the training hyperparameters were inherited from [8, 56], including the anchor boxes \mathbf{A} and the loss weights w , λ_{obj} , λ_{box} , and λ_{cls} . Others, including the keypoint bounding box size b_s and the keypoint loss weight λ_{kps} , were manually tuned using a small grid search. The influence of b_s is studied in Section 4.3. The models were trained on four V100 GPUs with 32 GB memory each using batch sizes of 128, 72, and 48 for KAPAO-S, KAPAO-M, and KAPAO-L, respectively. Validation was performed after every epoch, saving the model weights that provided the highest validation AP.

Testing. The inference parameters (τ_{cp} , τ_{ck} , τ_{bp} , τ_{bk} , τ_{fd} , and τ_{fc}) were manually tuned on the validation set. For TTA, we scale the input image by factors of 0.8, 1, and 1.2, and horizontally flip the unscaled image. During post-processing, the multi-scale detections are concatenated before running NMS. When not using TTA, we feed the network rectangular images (i.e., 1280 px on the longest side), which marginally reduces the accuracy but increases the inference speed.

Results. Table 1 compares the accuracy and latency (sum of forward pass and post-processing) of KAPAO with state-

¹More details available at <https://cocodataset.org/#keypoints-eval>.

Method	TTA	Input Size(s)	Parameters (M)	Forward Pass (ms)	Post-Proc. (ms)	Latency (ms)	AP	AR
HigherHRNet-W32 [6]	N	512	28.6	46.1	50.1	96.2	63.6	69.0
HigherHRNet-W32 [6]	N	640	28.6	52.4	71.4	124	64.9	70.3
HigherHRNet-W48 [6]	N	640	63.8	75.4	59.2	135	66.6	71.5
DEKR-W32 [11]	N	512	29.6	62.6	34.9	97.5	62.4	69.6
DEKR-W48 [11]	N	640	65.7	109	45.8	155	66.3	73.2
KAPAO-S	N	1280	12.6	14.7	2.80	17.5	63.0	70.2
KAPAO-M	N	1280	35.8	30.7	2.88	33.5	68.5	75.5
KAPAO-L	N	1280	77.0	51.3	3.07	54.4	70.6	77.4
HigherHRNet-W32 [6]	Y	256, 512, 1024	28.6	365	372	737	69.9	74.3
HigherHRNet-W32 [6]	Y	320, 640, 1280	28.6	431	447	878	70.6	75.0
HigherHRNet-W48 [6]	Y	320, 640, 1280	63.8	643	436	1080	72.1	76.1
DEKR-W32 [11]	Y	256, 512, 1024	29.6	552	137	689	70.5	76.2
DEKR-W48 [11]	Y	320, 640, 1280	65.7	1010	157	1170	72.1	77.8
KAPAO-S	Y	1024, 1280, 1536	12.6	61.5	3.70	65.2	64.4	71.5
KAPAO-M	Y	1024, 1280, 1536	35.8	126	3.67	130	69.9	76.8
KAPAO-L	Y	1024, 1280, 1536	77.0	211	3.70	215	71.6	78.5

Table 1. Accuracy and speed comparison with state-of-the-art single-stage human pose estimation models on COCO `val2017`, including the forward pass and post-processing. Latencies averaged over `val2017` using a batch size of 1 on a TITAN Xp GPU.

of-the-art single-stage methods DEKR [11] and HigherHRNet [6] on `val2017`. All latencies were measured on the same machine using a TITAN Xp GPU and batch size of 1. Since KAPAO does not use heatmaps, post-processing requires ~ 1 to 2 orders of magnitude less time than DEKR and HigherHRNet. When not using TTA, KAPAO-L is $2.5 \times$ faster and 4.0 AP more accurate than the next best model HigherHRNet-W48. When using TTA, KAPAO-L provides competitive AP, state-of-the-art AR, and is roughly $5 \times$ faster than both DEKR-48 and HigherHRNet-W48.

In Table 2, we compare the accuracy of KAPAO with single-stage and two-stage methods on `test-dev`. KAPAO-L achieves state-of-the-art AR and falls within 0.2 AP of previous single-stage methods, noting that DEKR uses a model-agnostic rescoring network that adds ~ 0.5 AP [11]. Compared to previous single-stage methods, KAPAO-L provides higher AP at low OKS thresholds (*e.g.*, AP⁵⁰) but lower AP at high OKS thresholds (*e.g.*, AP⁷⁵), which is indicative of better detection rates but less precise keypoint localization. We consider this an area to explore in future work.

4.2. CrowdPose

CrowdPose [25] is a curated multi-person human pose estimation dataset comprising images of crowded scenes with heavy occlusion. Top-down methods (*e.g.*, AlphaPose [9] and Mask-RCNN [15]) typically perform worse on CrowdPose as person detections with multiple people are problematic for the subsequent keypoint estimation. MIPNet [21] is an exception, as the authors explicitly address the aforementioned problem in their top-down approach.

The CrowdPose dataset contains 20k images and 80k person instances with 14 labeled keypoints ($K=14$). As

Method	AP	AP ⁵⁰	AP ⁷⁵	AP ^M	AP ^L	AR
CPN [5] [†]	72.1	91.4	80.0	68.7	77.2	78.5
SimpleBaseline [60] [†]	73.7	91.9	81.1	70.3	80.0	79.0
HRNet-W48 [49] [†]	75.5	92.5	83.3	71.9	81.5	80.5
EvoPose2D-L [33] [†]	75.7	91.9	83.1	72.2	81.5	81.7
MIPNet [21] [†]	75.7	-	-	-	-	-
RLE [24] [†]	75.7	92.3	82.9	72.3	81.3	-
OpenPose [4]	61.8	84.9	67.5	57.1	68.2	66.5
Mask-RCNN [15]	63.1	87.3	68.7	57.8	71.4	-
Associative Embeddings [38]	65.5	86.8	72.3	60.6	72.6	70.2
PersonLab [41]	68.7	89.0	75.4	64.1	75.5	75.4
SPM [40]	66.9	88.5	72.9	62.6	73.1	-
PifPaf [22]	66.7	-	-	62.4	72.9	-
HigherHRNet-W48 [6]	70.5	89.3	77.2	66.6	75.8	74.9
DEKR-W48 [11]	71.0	89.2	78.0	67.1	76.9	76.7
KAPAO-S	63.8	88.4	70.4	58.6	71.7	71.2
KAPAO-M	68.8	90.5	76.5	64.3	76.0	76.3
KAPAO-L	70.3	91.2	77.8	66.3	76.8	77.7

Table 2. Accuracy comparison with two-stage ([†]) and single-stage methods on COCO `test-dev`, including TTA. DEKR results use a model-agnostic rescoring network [11].

in [6, 11], we train on the `trainval` split with 12k images, and evaluate on the 8k images in `test`. We use the same training and inference settings as on COCO except we train for 300 epochs instead of 500 and we do not perform any validation. The final model weights are used for testing. The dataset accuracy metrics are similar to COCO and include AP, AP⁵⁰, and AP⁷⁵. AP^E, AP^M, and AP^H are additionally considered for images with easy, medium, and hard *Crowd Index*, as assigned by the dataset creators [25].

Table 3 compares the accuracy of KAPAO against state-

Method	AP	AP ⁵⁰	AP ⁷⁵	AP ^E	AP ^M	AP ^H
AlphaPose [9] [†]	61.0	81.3	66.0	71.2	61.4	51.1
MIPNet [21] [†]	70.0	-	-	-	-	-
Mask-RCNN [15]	57.2	83.5	60.3	69.4	57.9	45.8
OpenPose [4]	-	-	-	62.7	48.7	32.3
SPPE [25]	66.0	84.2	71.5	75.5	66.3	57.4
HigherHRNet-W48 [6]	67.6	87.4	72.6	75.8	68.1	58.9
DEKR-W48 [11]	68.0	85.5	73.4	76.6	68.8	58.4
KAPAO-S	63.8	87.7	69.4	72.1	64.8	53.2
KAPAO-M	67.1	88.8	73.4	75.2	68.1	56.9
KAPAO-L	68.9	89.4	75.6	76.6	69.9	59.5

Table 3. Accuracy comparison with single-stage and two-stage ([†]) methods on CrowdPose `test`, including TTA. DEKR results use a model-agnostic rescore network [11].

of-the-art methods. We find that KAPAO excels in the presence of occlusion, improving upon all previous single-stage methods across all metrics. KAPAO’s proficiency in crowded scenes is clear when analyzing AP^E, AP^M, and AP^H: KAPAO-L and DEKR-W48 [11] perform equally on images with easy Crowd Index (less occlusion), but KAPAO-L is 1.1 AP more accurate for both medium and hard Crowd Indexes (more occlusion).

4.3. Ablation Studies

We empirically analyze the influence of one of KAPAO’s important hyperparameters: the keypoint bounding box size b_s . Five KAPAO-S models were trained on COCO `train2017` for 50 epochs using normalized keypoint bounding box sizes $b_s/w \in \{0.01, 0.025, 0.05, 0.075, 0.1\}$. The validation AP is plotted in Figure 5. Our results are consistent with the prior work of McNally *et al.* [34]: $b_s/w < 2.5\%$ destabilizes training leading to poor accuracy, and optimal b_s/w is observed around 5% (used in Section 4 experiments). Contrary to McNally *et al.*, our accuracy degrades quickly for $b_s/w > 5\%$. We hypothesize that large b_s in our application interferes with pose object learning.

The accuracy improvements resulting from fusing the keypoint objects with the pose objects are provided in Table 4. Keypoint object fusion adds no less than 1.0 AP and over 3.0 AP in some cases. Moreover, keypoint object fusion is fast; the added post-processing time per image is ≤ 1.7 ms on COCO and ≤ 4.5 ms on CrowdPose. Relative to the time required for the forward pass of the network, these are small increases.

Finally, we study the fusion of keypoint objects by class. Figure 6 plots the fusion rates for each keypoint type for KAPAO-S with no TTA on COCO `val2017`. The fusion rate is equal to the number of fused keypoint objects divided by the number of keypoints of that type in the dataset. Because the number of human pose predictions is generally greater than the actual number of person instances in the dataset, the fusion rate can be greater than 1. As origi-

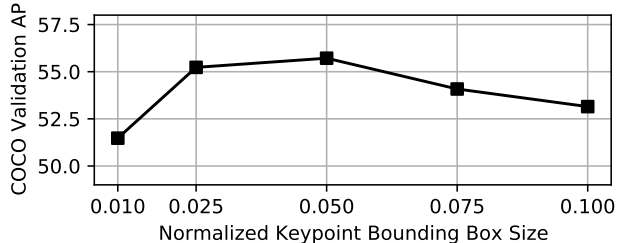


Figure 5. The influence of keypoint object bounding box size on learning. Each KAPAO-S model was trained for 50 epochs.

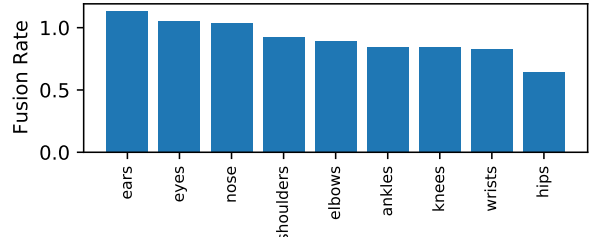


Figure 6. Keypoint object fusion rates for each keypoint type. Evaluated on COCO `val2017` using KAPAO-S without TTA.

Method	TTA	Δ Lat. (ms) / Δ AP (COCO <code>val2017</code>)	Δ Lat. (ms) / Δ AP (CrowdPose <code>test</code>)
KAPAO-S	N	+1.2 / +2.4	+3.3 / +2.9
KAPAO-M	N	+1.2 / +1.1	+3.5 / +3.2
KAPAO-L	N	+1.7 / +1.2	+4.2 / +1.0
KAPAO-S	Y	+1.7 / +2.8	+3.9 / +3.2
KAPAO-M	Y	+1.6 / +1.5	+4.4 / +3.5
KAPAO-L	Y	+1.4 / +1.1	+4.5 / +1.0

Table 4. Accuracy improvement when fusing keypoint object detections with human pose detections. Latencies averaged over each dataset using a batch size of 1 on a TITAN Xp GPU.

nally hypothesized, keypoints that are characterized by distinct local image features (*e.g.*, the eyes, ears, and nose) have higher fusion rates as they are detected more precisely as keypoint objects than as pose objects. Conversely, keypoints that require a more global understanding (*e.g.*, the hips) are better detected using pose objects, as evidenced by lower fusion rates.

5. Conclusion

This paper presents KAPAO, a new heatmap-free keypoint estimation method based around modeling *keypoints and poses as objects*. We conclude that KAPAO can be effectively applied to the problem of single-stage multi-person human pose estimation by detecting human pose objects directly. Moreover, fusing jointly detected keypoint objects improves the accuracy of the predicted human poses with minimal computational overhead. As a result, KAPAO is significantly faster than previous single-stage methods, which are impeded by heatmap post-processing

and bottom-up keypoint grouping. When not using test-time augmentation, KAPAO is considerably more accurate than the state-of-the-art. Moreover, KAPAO performs well in the presence of heavy occlusion, as evidenced by new state-of-the-art accuracy for a single-stage method on CrowdPose.

Acknowledgements. This work was supported in part by Compute Canada, the Canada Research Chairs Program, the Natural Sciences and Engineering Research Council of Canada, a Microsoft Azure Grant, and an NVIDIA Hardware Grant.

References

- [1] Mykhaylo Andriluka, Umar Iqbal, Eldar Insafutdinov, Leonid Pishchulin, Anton Milan, Juergen Gall, and Bernt Schiele. Posetrack: A benchmark for human pose estimation and tracking. In *CVPR*, 2018. 1
- [2] Alexey Bochkovskiy, Chien-Yao Wang, and Hong-Yuan Mark Liao. Yolov4: Optimal speed and accuracy of object detection. *arXiv preprint arXiv:2004.10934*, 2020. 2, 3, 6
- [3] Zhaowei Cai and Nuno Vasconcelos. Cascade R-CNN: Delving into high quality object detection. In *CVPR*, 2018. 3
- [4] Zhe Cao, Tomas Simon, Shih-En Wei, and Yaser Sheikh. Realtime multi-person 2d pose estimation using part affinity fields. In *CVPR*, 2017. 1, 2, 3, 7, 8
- [5] Yilun Chen, Zhicheng Wang, Yuxiang Peng, Zhiqiang Zhang, Gang Yu, and Jian Sun. Cascaded pyramid network for multi-person pose estimation. In *CVPR*, 2018. 1, 2, 3, 7
- [6] Bowen Cheng, Bin Xiao, Jingdong Wang, Honghui Shi, Thomas S Huang, and Lei Zhang. HigherHRNet: Scale-aware representation learning for bottom-up human pose estimation. In *CVPR*, 2020. 1, 2, 3, 7, 8
- [7] Xuanyi Dong, Yan Yan, Wanli Ouyang, and Yi Yang. Style aggregated network for facial landmark detection. In *CVPR*, 2018. 1, 2
- [8] Glenn Jocher et. al. ultralytics/yolov5: v5.0, Apr. 2021. 2, 4, 5, 6
- [9] Hao-Shu Fang, Shuqin Xie, Yu-Wing Tai, and Cewu Lu. RMPE: Regional multi-person pose estimation. In *ICCV*, 2017. 7, 8
- [10] Kirill Gavrilyuk, Ryan Sanford, Mehrsan Javan, and Cees GM Snoek. Actor-transformers for group activity recognition. In *CVPR*, 2020. 1
- [11] Zigang Geng, Ke Sun, Bin Xiao, Zhaoxiang Zhang, and Jingdong Wang. Bottom-up human pose estimation via disentangled keypoint regression. In *CVPR*, 2021. 1, 2, 3, 7, 8
- [12] Ross Girshick. Fast R-CNN. In *ICCV*, 2015. 3
- [13] Ross Girshick, Jeff Donahue, Trevor Darrell, and Jitendra Malik. Rich feature hierarchies for accurate object detection and semantic segmentation. In *CVPR*, 2014. 3
- [14] Priya Goyal, Piotr Dollár, Ross Girshick, Pieter Noordhuis, Lukasz Wesolowski, Aapo Kyrola, Andrew Tulloch, Yangqing Jia, and Kaiming He. Accurate, large mini-batch sgd: Training imagenet in 1 hour. *arXiv preprint arXiv:1706.02677*, 2017. 6
- [15] Kaiming He, Georgia Gkioxari, Piotr Dollár, and Ross Girshick. Mask R-CNN. In *ICCV*, 2017. 3, 7, 8
- [16] Weiting Huang, Pengfei Ren, Jingyu Wang, Qi Qi, and Haifeng Sun. Awr: Adaptive weighting regression for 3d hand pose estimation. In *AAAI*, 2020. 1, 2
- [17] Umar Iqbal, Pavlo Molchanov, Thomas Breuel Juergen Gall, and Jan Kautz. Hand pose estimation via latent 2.5 d heatmap regression. In *ECCV*, 2018. 1, 2
- [18] Tomas Jakab, Ankush Gupta, Hakan Bilen, and Andrea Vedaldi. Unsupervised learning of object landmarks through conditional image generation. In *NeurIPS*, 2018. 1
- [19] Sangryul Jeon, Dongbo Min, Seungryong Kim, and Kwanghoon Sohn. Joint learning of semantic alignment and object landmark detection. In *ICCV*, 2019. 4
- [20] Alex Kendall and Yarin Gal. What uncertainties do we need in bayesian deep learning for computer vision? In *NeurIPS*, 2017. 3
- [21] Rawal Khirodkar, Visesh Chari, Amit Agrawal, and Ambrish Tyagi. Multi-hypothesis pose networks: Rethinking top-down pose estimation. In *ICCV*, 2021. 1, 2, 3, 7, 8
- [22] Sven Kreiss, Lorenzo Bertoni, and Alexandre Alahi. Pifpf: Composite fields for human pose estimation. In *CVPR*, 2019. 3, 7
- [23] Yann LeCun, Yoshua Bengio, et al. Convolutional networks for images, speech, and time series. *The handbook of brain theory and neural networks*, 3361(10), 1995. 1
- [24] Jiefeng Li, Siyuan Bian, Ailing Zeng, Can Wang, Bo Pang, Wentao Liu, and Cewu Lu. Human pose regression with residual log-likelihood estimation. In *ICCV*, 2021. 2, 3, 7
- [25] Jiefeng Li, Can Wang, Hao Zhu, Yihuan Mao, Hao-Shu Fang, and Cewu Lu. Crowdpose: Efficient crowded scenes pose estimation and a new benchmark. In *CVPR*, 2019. 3, 6, 7, 8
- [26] Ke Li, Shijie Wang, Xiang Zhang, Yifan Xu, Weijian Xu, and Zhuowen Tu. Pose recognition with cascade transformers. In *CVPR*, 2021. 2, 3
- [27] Yanjie Li, Sen Yang, Shoukui Zhang, Zhicheng Wang, Wankou Yang, Shu-Tao Xia, and Erjin Zhou. Is 2d heatmap representation even necessary for human pose estimation? *arXiv preprint arXiv:2107.03332*, 2021. 2
- [28] Tsung-Yi Lin, Piotr Dollár, Ross Girshick, Kaiming He, Bharath Hariharan, and Serge Belongie. Feature pyramid networks for object detection. In *CVPR*, 2017. 4
- [29] Tsung-Yi Lin, Priya Goyal, Ross Girshick, Kaiming He, and Piotr Dollár. Focal loss for dense object detection. In *ICCV*, 2017. 3
- [30] Tsung-Yi Lin, Michael Maire, Serge Belongie, James Hays, Pietro Perona, Deva Ramanan, Piotr Dollár, and C Lawrence Zitnick. Microsoft COCO: Common objects in context. In *ECCV*, 2014. 6
- [31] Wei Liu, Dragomir Anguelov, Dumitru Erhan, Christian Szegedy, Scott Reed, Cheng-Yang Fu, and Alexander C Berg. Ssd: Single shot multibox detector. In *ECCV*, 2016. 3
- [32] Ilya Loshchilov and Frank Hutter. SGDR: Stochastic gradient descent with warm restarts. In *ICLR*, 2017. 6
- [33] William McNally, Kanav Vats, Alexander Wong, and John McPhee. EvoPose2D: Pushing the boundaries of 2d human pose estimation using accelerated neuroevolution with weight transfer. *IEEE Access*, 2021. 1, 2, 3, 7

[34] William McNally, Pascale Walters, Kanav Vats, Alexander Wong, and John McPhee. DeepDarts: Modeling keypoints as objects for automatic scorekeeping in darts using a single camera. In *CVPRW*, 2021. 1, 2, 3, 4, 8

[35] William McNally, Alexander Wong, and John McPhee. Action recognition using deep convolutional neural networks and compressed spatio-temporal pose encodings. *Journal of Computational Vision and Imaging Systems*, 4(1), 2018. 1

[36] William McNally, Alexander Wong, and John McPhee. STAR-Net: Action recognition using spatio-temporal activation reprojection. In *CRV*, 2019. 1

[37] Yurii Nesterov. A method for solving the convex programming problem with convergence rate $o(1/k^2)$. *Proceedings of the USSR Academy of Sciences*, 269:543–547, 1983. 6

[38] Alejandro Newell, Zhiao Huang, and Jia Deng. Associative embedding: End-to-end learning for joint detection and grouping. In *NeurIPS*, 2017. 3, 7

[39] Alejandro Newell, Kaiyu Yang, and Jia Deng. Stacked hourglass networks for human pose estimation. In *ECCV*, 2016. 1, 2, 3

[40] Xuecheng Nie, Jiashi Feng, Jianfeng Zhang, and Shuicheng Yan. Single-stage multi-person pose machines. In *ICCV*, 2019. 3, 7

[41] George Papandreou, Tyler Zhu, Liang-Chieh Chen, Spyros Gidaris, Jonathan Tompson, and Kevin Murphy. Personlab: Person pose estimation and instance segmentation with a bottom-up, part-based, geometric embedding model. In *ECCV*, 2018. 7

[42] Dario Pavllo, Christoph Feichtenhofer, David Grangier, and Michael Auli. 3d human pose estimation in video with temporal convolutions and semi-supervised training. In *CVPR*, 2019. 1

[43] Yaadhav Raaj, Haroon Idrees, Gines Hidalgo, and Yaser Sheikh. Efficient online multi-person 2d pose tracking with recurrent spatio-temporal affinity fields. In *CVPR*, 2019. 1

[44] Joseph Redmon, Santosh Divvala, Ross Girshick, and Ali Farhadi. You only look once: Unified, real-time object detection. In *CVPR*, 2016. 2, 3

[45] Joseph Redmon and Ali Farhadi. Yolo9000: better, faster, stronger. In *CVPR*, 2017. 2, 3

[46] Joseph Redmon and Ali Farhadi. Yolov3: An incremental improvement. *arXiv preprint arXiv:1804.02767*, 2018. 2, 3

[47] Shaoqing Ren, Kaiming He, Ross Girshick, and Jian Sun. Faster R-CNN: Towards real-time object detection with region proposal networks. *arXiv preprint arXiv:1506.01497*, 2015. 3

[48] Danilo Rezende and Shakir Mohamed. Variational inference with normalizing flows. In *ICML*, 2015. 3

[49] Ke Sun, Bin Xiao, Dong Liu, and Jingdong Wang. Deep high-resolution representation learning for human pose estimation. In *CVPR*, 2019. 1, 2, 3, 7

[50] Supasorn Suwajanakorn, Noah Snavely, Jonathan Tompson, and Mohammad Norouzi. Discovery of latent 3d keypoints via end-to-end geometric reasoning. In *NeurIPS*, 2018. 1

[51] Jonathan J Tompson, Arjun Jain, Yann LeCun, and Christoph Bregler. Joint training of a convolutional network and a graphical model for human pose estimation. In *NeurIPS*, 2014. 1, 2

[52] Alexander Toshev and Christian Szegedy. DeepPose: Human pose estimation via deep neural networks. In *CVPR*, 2014. 2

[53] Roberto Valle, José M Buenaposada, Antonio Valdés, and Luis Baumela. Face alignment using a 3d deeply-initialized ensemble of regression trees. *Computer Vision and Image Understanding*, 189:102846, 2019. 2

[54] Kanav Vats, William McNally, Chris Duhanty, Zhong Qiu Lin, David A Clausi, and John Zelek. PuckNet: Estimating hockey puck location from broadcast video. In *AAAI Workshops*, 2019. 2

[55] Roman Voeikov, Nikolay Falaleev, and Ruslan Baikulov. Ttnet: Real-time temporal and spatial video analysis of table tennis. In *CVSports*, 2020. 1

[56] Chien-Yao Wang, Alexey Bochkovskiy, and Hong-Yuan Mark Liao. Scaled-yolov4: Scaling cross stage partial network. *arXiv preprint arXiv:2011.08036*, 2020. 2, 3, 4, 5, 6

[57] Chien-Yao Wang, Hong-Yuan Mark Liao, Yueh-Hua Wu, Ping-Yang Chen, Jun-Wei Hsieh, and I-Hau Yeh. Cspnet: A new backbone that can enhance learning capability of cnn. In *CVPR*, 2020. 4

[58] Xinyao Wang, Liefeng Bo, and Li Fuxin. Adaptive wing loss for robust face alignment via heatmap regression. In *ICCV*, 2019. 1, 2

[59] Shih-En Wei, Varun Ramakrishna, Takeo Kanade, and Yaser Sheikh. Convolutional pose machines. In *CVPR*, 2016. 2, 3

[60] Bin Xiao, Haiping Wu, and Yichen Wei. Simple baselines for human pose estimation and tracking. In *ECCV*, 2018. 1, 2, 3, 7

[61] Zixuan Xu, Banghuai Li, Ye Yuan, and Miao Geng. AnchorFace: An anchor-based facial landmark detector across large poses. In *AAAI*, 2021. 1, 2, 3, 4

[62] Sen Yang, Zhibin Quan, Mu Nie, and Wankou Yang. Transpose: Keypoint localization via transformer. In *ICCV*, 2021. 1, 2

[63] Zhaohui Zheng, Ping Wang, Wei Liu, Jinze Li, Rongguang Ye, and Dongwei Ren. Distance-iou loss: Faster and better learning for bounding box regression. In *AAAI*, 2020. 5

[64] Xingyi Zhou, Dequan Wang, and Philipp Krähenbühl. Objects as points. *arXiv preprint arXiv:1904.07850*, 2019. 1